

1

2 **Supplementary Information for**

3 **Active entanglement enables stochastic, topological grasping**

4 **Kaitlyn Becker, Clark Teeple, Nicholas Charles, Yeonsu Jung, Daniel Baum, James C. Weaver, L. Mahadevan, and Robert**
5 **Wood**

6 **Corresponding Author name.**

7 **E-mail: rjwood@g.harvard.edu & lmahadev@g.harvard.edu**

8 **This PDF file includes:**

- 9 Supplementary text
- 10 Figs. S1 to S10
- 11 Tables S1 to S2
- 12 Legends for Movies S1 to S2
- 13 SI References

14 **Other supplementary materials for this manuscript include the following:**

- 15 Movies S1 to S2

Supporting Information Text

Entanglement characterization. To quantify the degree of entanglement achieved with our filament actuators, we used a micro-CT scanner to image actuated arrays of filaments with and without grasped objects as shown in Figure 1 of the main text. Inside the micro-CT scanner, a fully plastic twelve-filament manifold was securely mounted on top of a stack of styrofoam rings with an interior diameter of 250 mm and sufficient vertical clearance for the actuated filaments to hover above the rotating platform of the scanner. The largely x-ray transparent foam rings provided a support structure above the rotating platform while minimizing added visual artifacts during the scan. The base of the ring stack was also securely mounted to the rotating platform. The filaments were first actuated (with or without an object) and then gently placed inside the styrofoam support structure mounted to an XRA-002 X-Tek micro-CT system for image data collection. A pneumatic tether supplied 172 kPa of pressure throughout each of the 30-minute scans in order to minimize sample drift. The 3D reconstructions were performed using CT-Pro (Nikon Metrology, Tring, UK) and were exported as a set of 16-bit gray-scale images for further processing. A commercial software package, Amira (Thermo Fisher Scientific, Waltham MA, USA), was used to segment the raw CT data (Figure S1A), separating individual filaments, grasped objects, and the manifold. Amira was used to trace the center line of the filaments, and extract a vector of the filament position, as shown in green in Figure S1B, with spheres marking the end point of each filament. These data were then used to separate each unique filament, as shown in Figure S1C, and to calculate the spatial density and local entanglement, as described below.

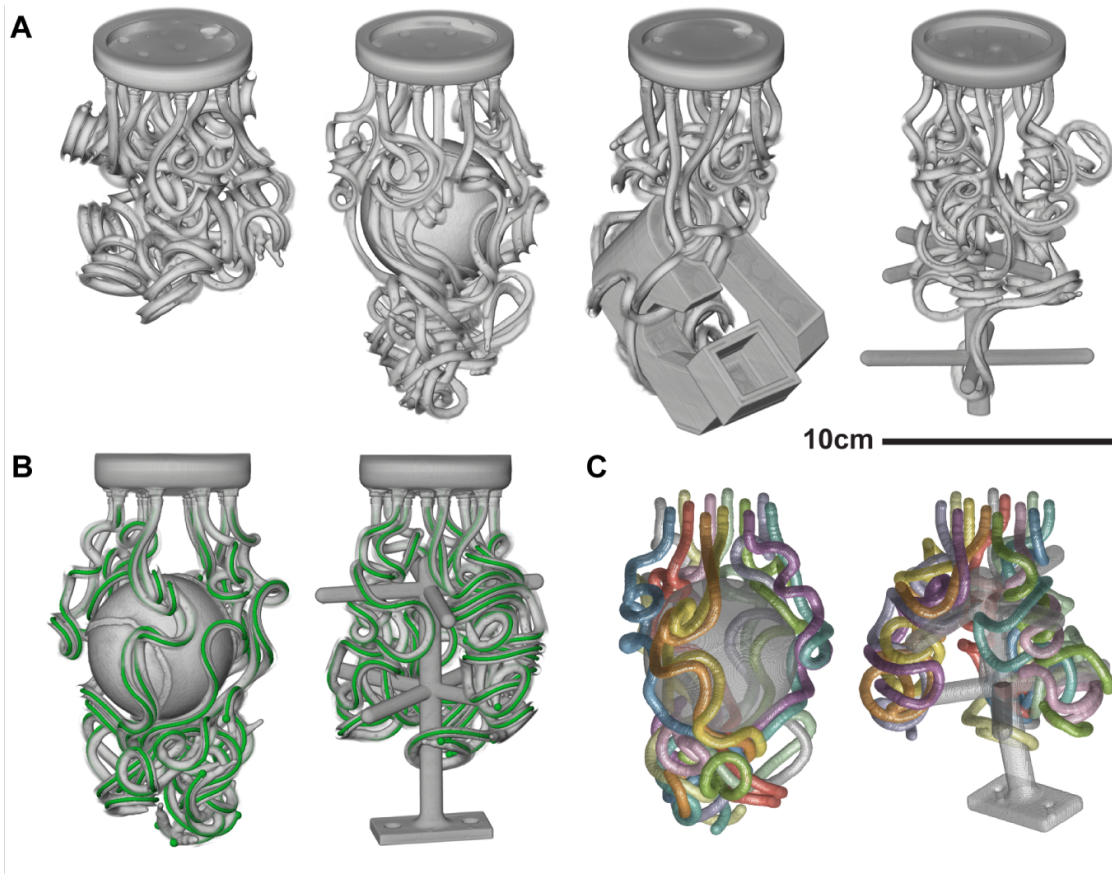


Fig. S1. micro-CT data and processing. Examples of the (A) globally segmented micro-CT data of filaments tangled with no object, with a sphere, with bar clamp adversarial object, and with the **eight-branch tree**. (B) Examples of the secondary segmentation of the micro-CT data to trace the filament positions (highlighted in green). (C) Visualization of the entanglement mass segmented and colored by individual filaments.

To quantify the spatial density and local entanglement of the arrays, as shown in Figure 2, we defined a spherical volume Ω at a point, \mathbf{r} , with the diameter of l , that is, $\Omega = \Omega(\mathbf{r}, l) = \{\mathbf{r}' | \|\mathbf{r}' - \mathbf{r}\| < l\}$ (Fig. 1D). at each point, \mathbf{r} , the number of filaments, n , was calculated by counting the unique filaments in Ω . The localized average crossing number, e , in Ω is given by the sum of all ACN between distinct pairs of filaments, that is, $\sum_{\alpha, \beta} e_{\alpha\beta}$, where α and β stand for two distinct parameterized curves that reside in Ω .

By definition, n and e should depend on \mathbf{r} and l . If the size, l , was comparable to the filament diameter (4 mm), it would not capture how many other filaments are contained in Ω . On the other hand, if l was large enough to cover the entire system, we could not see any density variation. An appropriate definition of n and e should enable us to understand how the localized variables vary over the scanned volume. One possible way is to use geometric mean between the filament diameter and the filament length: $\sqrt{4 \times 300} \approx 20$. Thus we used $l = 20$ mm throughout the present work.

Object Set and Grasp Testing. The object set used for the experimental testing in this study is shown in Figure S2A.

The tube and sphere were selected to represent a few variants on simple geometric primitives, reminiscent of the YCB object set (1). YCB is now an older object set but represents a seminal collection of objects used to standardize evaluation of robotic grasping performance. The sphere was 100 mm in diameter and 10 g in weight. The tube used for testing in the main text was 38 mm in diameter and 91 g in weight. Two additional tubes were used for testing below, one being 25 mm in diameter and 43 g in weight, the other being 64 mm in diameter and 103 g in weight. All tubes were 300 mm long and 1.6 mm thick. These simple object primitives were used to evaluate the grasp success rate when the robot arm lowered a filament gripper over a target object with ideal centering as well as with progressively increasing centering offset. In these tests, an offset between the vertical center axis of the gripper and target object was increased by 1 cm increments to evaluate the sensitivity of centering errors, following procedures outline in the work of Aukes (2) and Sinatra (3).

Four objects identified as part of an adversarial object set by Mahler et al. (Fig. S2B) were included as representative challenging target objects identified in robotic grasping literature (4). The four examples of adversarial objects shown in the bottom of Figure S2 were printed in poly-lactic acid (PLA) on a Prusa i3 MKS+ printer (Prusa Research, Prague, Czech Republic). From left to right, in the work by Mahler et al., the objects are called a bar clamp, motor mount, mount 2, and climbing hold. Mahler et al. tested objects in the various orientations that may occur if the object is dropped on a surface and the probability of each resulting orientation was computed (4). For the grasp testing in this work, the top four most probable orientations were each used for 20 grasping trials and the resulting success rate shown in Figure 2B of the main text was calculated as a weighted average of the 80 trials according to the relative probabilities of each orientation. The markings on the objects in Figure S2 were used to consistently place the objects in the four orientations underneath the robot arm for testing.

The test tree (eight-branch tree, Fig. S2A) was also introduced as a target object for testing that was more topologically complex than spheres, cubes, and cylindrical primitives. At the same time, the test tree structure was designed to be tractable to incorporate into the ACN metric of entanglement as described above, reproducible on widely available fused filament fabrication (FFF) printers, definable in the simulation framework described below, and simple enough to be implemented in simulations with relatively low computational cost. The dimensions of the standard test tree include the trunk height of 120 mm, trunk diameter of 10 mm, branch length of 50 mm, branch diameter of 7 mm, and location of branching points at 60 mm and 105 mm (from the bottom of trunk to the bottom of the branches). The eight-branch tree has eight branches (though a four-branch version is also shown in Figure S6). The majority of tests were performed with the eight-branch tree with branches at a 90 degree angle to the trunk, though a small set of tests represented in Figure S5 included variants of the eight-branch tree with branched angled upward or downward at 45 degrees. The length of the branches of the standard eight-branch tree with horizontal branches were varied to explore grasping success sensitivity to object spatial density, as described in the main text. Varying masses were also added to the base of the tree for the experiments regarding sensitivity to object mass.

The mass of the object as compared to the friction of the filaments plays a role in the release of a target object. This was not a focus of the current study, however we observed approximately 10 instances in 950 successful grasps where the filaments did not immediately release an object. Most of these instances occurred with the lightest test tree and all were resolved by cycling the filament pressure once. Lubrication will also have a large effect, whether the filaments are intentionally coated or working in an aqueous or perhaps dusty environment. Additionally, we observed that, because the filaments were fabricated in a straight form factor and the rubber is not experiencing plastic deformation, the filaments spring back to a mostly straight form upon the return to gauge pressure. Springing to a straight and streamlined shape makes the filaments more likely to disengage, as opposed to reducing stiffness after returning to gauge pressure but remaining in a highly curled configuration. Prior to entanglement, the filaments start at a similar height to one another, with a roughly parallel orientation. With the top of the filaments constrained and undergoing relatively little shear motion, their entangled configurations are easily reversible. There is also minimal tension applied to the filament ends when they are approaching and pulling away from an object, likely reducing the probability of the filaments tying themselves into knots when approaching or pulling away from an object.

In addition to the set of objects used for laboratory and simulation grasp tests, the gripper was tested under water, in a five gallon fresh water laboratory tank as well, as using a remotely operated arm and an ROV in a series of deep-sea salt water field tests. In both cases, the filaments were hydraulically actuated. Ocean-based testing adds the complications of a different surrounding fluid, currents, unpredictable target objects, and limited testing vision and feedback. To encourage the filaments to drape around target objects and settle between movements of the ROV arm, small weights, (6 mm long and 1.6 mm steel pins), were encapsulated in the distal ends of the filaments. A twelve-filament array like the set used for the laboratory and simulated grasp success testing was successfully used to pick up and release objects at a depths reaching 800 m. The field tests were performed with the help of the Schmidt Ocean Institute, the crew of the Falkor, the ROV pilots operating the vehicle SuBastien, and our collaborators from the URIL (Undersea Robotics & Imaging Laboratory) lab at the University of Rhode Island. Development of the entanglement gripper was originally motivated by the challenging grasping tasks in the deep-sea, where the gentle grasps of deep-sea life and precious artifacts cannot be done by human hands due to the hydrostatic pressure.

While the filament gripper was originally inspired by challenging deep-sea grasping tasks, the authors believe that entanglement grasping can also augment the abilities of robotic grasping with everyday objects on land which is the primary focus of this work. As discussed above, we have begun initial testing with a small subset of target objects. Rigorous testing with more complex objects, as well as discussion of how to classify the complexity of objects will be a subject of future study. The set of objects in Figure S3 is intended to demonstrate the feasibility of using entanglement grasping for familiar household objects that might prove more challenging for the vast majority of robotic grippers, including an array of houseplants, irregularly

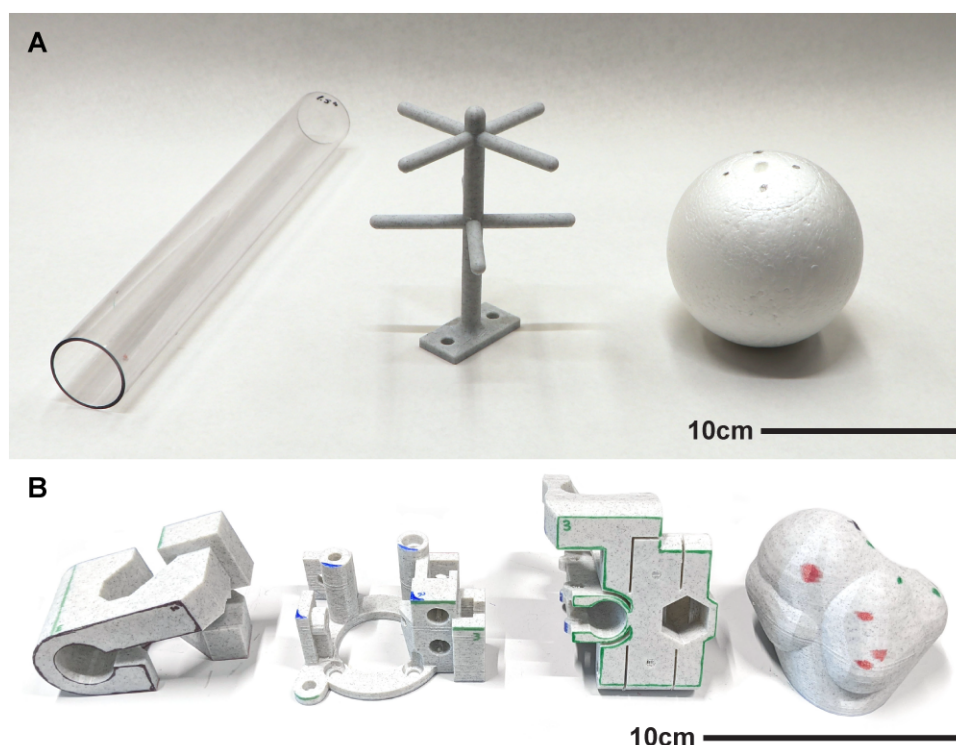


Fig. S2. Set of target objects used in testing. (A) Tube (38 mm OD), eight-branch tree, and sphere used for experimental testing. Not shown are the added weights that were attached to the bottom of the tree structures for the robot arm grasp tests. (B) Four sample adversarial objects from the work of Mahler et al. that were used in experimental testing. From left to right, the objects are called a bar clamp, motor mount, mount 2, and climbing hold (4). The markings visible on the objects were used to guide object orientation and placement in testing.

shaped toys, and a flexible phone tripod. The grasping demonstrations below were not performed with a robot arm. To emulate a top drape approach while allowing the gripper to remain in a static position, the object was manually raised up into the array of unactuated filaments and the filaments were then pneumatically actuated around the object with an operating pressure of 25 psi (172 kPa). With an exception of the begonia in the bottom right, all of the objects in Figure S3 were fully supported by the filament array in the photos.

Object Pull Tests. As presented in the main text, grasping force tests were performed on an Instron material testing machine. Photographs of the test setup (with a subset of the objects tested) are shown in figure S4 along with plots of the raw force versus extension data. The filaments started above the object and were then draped around the object using the vertical travel of the machine. The objects were also rigidly anchored, which was not true in the grasp success trials with the robot arm but the rigid anchoring provided a benchmark of the grip strength and toughness. A summary of the average maximum gripping values observed from each trial as well as the maximum observed value across all trials is summarized in Figure S5. Examples of the trial sets from which these values are derived, shown in Figure S4, include the eight-branch tree, the 63.5 mm diameter horizontally oriented tube, the 25.4 mm diameter vertically oriented tube, and the 63.5 mm diameter vertically oriented tube. As one might expect, the maximal gripping force achieved by the filament gripper was highly affected by the target object. Furthermore, the shape of the force versus extension curves shown in Figure S4 reflects the nature of the engagement between the filaments and the object. For example, the filaments predominantly rely on friction to hold the vertical tubes. As the object is pulled from the gripper, the forces in Figure S4C and Figure S4D are relatively level and show the friction forces as the object slides through the grasp of the filaments. By contrast, the trials from the eight-branch tree in Figure S4A and horizontal tube in Figure S4B appear to exhibit larger degrees of variation that related to how many of the filaments wrapped around the tube or branches in addition to wrapping around nearby filaments. There are also larger discrete jumps in the data as individual filaments are pulled away and forced to release the object.

Using the shape of the data to discover information about an object may be an interesting direction for future study with entanglement grasping platforms. An example that could be investigated in greater depth is a slight upward trend in the data of the 25.4 mm OD tube and a slight downward trend in the data of the 63.5 mm OD tube, which may possibly be explained by the way in which the filaments engage with the two objects. The testing setup associated with these two trial sets is shown in Figure S4D and Figure S4C. As shown in the pictures, the filaments were draped around the outside of the 25.4 mm tube but the 63.5 mm tube was large enough that they were lowered inside. As the filaments are pulled up from the object, their coils are extended, which would cause the coil diameter to contract and thereby cause a slight increase in forces as the filaments squeeze the outside of the smaller tube and decrease forces as the filaments pull away from the inner wall of the larger tube.



Fig. S3. Testing on some challenging objects.

Grasp Toughness Metric. For the proposed grasp toughness metric, we used a trapezoidal approximation to numerically integrate the area under the averaged force-displacement curves of the grasp strength tests, such as the ones shown in Figure S4. The comparison values for the grasp toughness of soft grippers were similarly calculated from the data sets presented in prior soft gripper work, including the four-finger gripper with added tips around a 76 mm tube from Abundance et al. (5), the two finger power grasp around a 51 mm tube from Teeple et al. (6), and the two finger power grasp (with foam) around a 51 mm tube from Galloway et al. (7). It should be noted that these literature values are low estimates owing to the fact that the raw grip tests trials were truncated to the shortest release in order to more easily calculate an average value.

Contact Distribution. Combining notions of toughness and entanglement forces with the spatial distribution of filaments, a separate set of 31 tests were also conducted to compare the measured toughness and peak forces to the contacts on an eight-branch tree, results of which are shown in Figure S4. We manually counted the number of filament-object contacts on the test tree for 31 of the pullout tests described above. For simplicity, the contacts were counted at the beginning of the test but not through the evolution of the test. It is important to note that the number of contacts with a target object does not alone affect entanglement robustness. The resulting force and toughness of each of the tests is plotted against the number of contacts in Figure S4 and the data readily show that grasps with relatively few contacts are able to impart higher forces and energy than grasps with more points of contact with the test tree. Thus, from the resulting data, it can be seen that the number of contacts with a target object does not alone affect entanglement robustness. Qualitatively, this was clear from observing filament configurations. Filaments that independently curled around separate branches of the tree, without interacting with other filament, each acted as weak coil springs. When filaments wrapped over one-another, achieving higher levels of entanglement, they are able to hold a branch more securely. The entangled collective strength is therefore greater than the sum of its parts.

Randomly distributed contact points is a distinguishing feature of entanglement grasping with the filament gripper, which are difficult and time consuming to quantify in physical experiments but relatively easy to pull out of the simulation environment. For comparison between simulations and physical testing, we manually counted contact points on a four and eight-branch tree object. The filament gripper was mounted onto a frame on top of a rotating platform and five photographs of the example grasps were taken at 45 deg increments, as shown in Figure S6. The camera remained stationary while the platform supporting the gripper and support structure were rotated. The objects were manually raised into the filaments to simulate a top drape approach with the fixed gripper mount. Two examples of the results are shown in Figure S6A and S6B. The contacts were grouped by filament, as indicated by the letter and color. Individual contact points were visible in multiple views and thus have the same labels that appear in multiple images.

The contacts from the pictured eight-branch tree grasp in Figure S6 are also shown in Figure 1B, next to an example of simulated grasp of an eight-branch tree. In those examples shown, fourteen contact points are made by eight of the twelve gripper filaments. The range of contact points observed from successful grasp simulations was 11 to 32 discrete points of contact. This range of contacts was pulled from the results from the grasp test simulations represented in Figure 3G. (This included trials with varying weights of the eight-branch tree, but not trials with varying branch lengths or varying filament spacing. So, this only included normalized branch lengths and spatial densities of one from Figure 3G in the main text.) Not

all contacts counted were necessarily load bearing, as can be inferred by the examples in Figure 1B and Figure S6, suggesting that, for a given filament strength, there is a critical threshold of engagement or contacts that leads to a successful grasp and that number of contact points increases with target object weight. We have observed successful grasps with lower numbers of contacts from physical testing, (as low as one or two contacts), but this is dependent on the object weight and static friction, and the latter is not represented in the simulation. The entanglement gripper performance and contact also changes with target object shape, which we intend to characterize further in future work.

While the contacts between filaments and the target object could be counted manually, it was not feasible to manually count the inter-filament contacts from photographs. From the micro-CT data, however, it was possible to isolate both surface contacts and contacts between filaments, as shown in Figure S6C, where red indicates object-filament contacts and blue indicates filament-filament contacts. As expected, the spatial arrangement of contacts is significantly affected by the object or lack of object with which the filaments interact. Both the contact points between the filaments, as well as the contacts between filaments and objects affects the stiffness and overall toughness of an assemblage of tangled filaments.

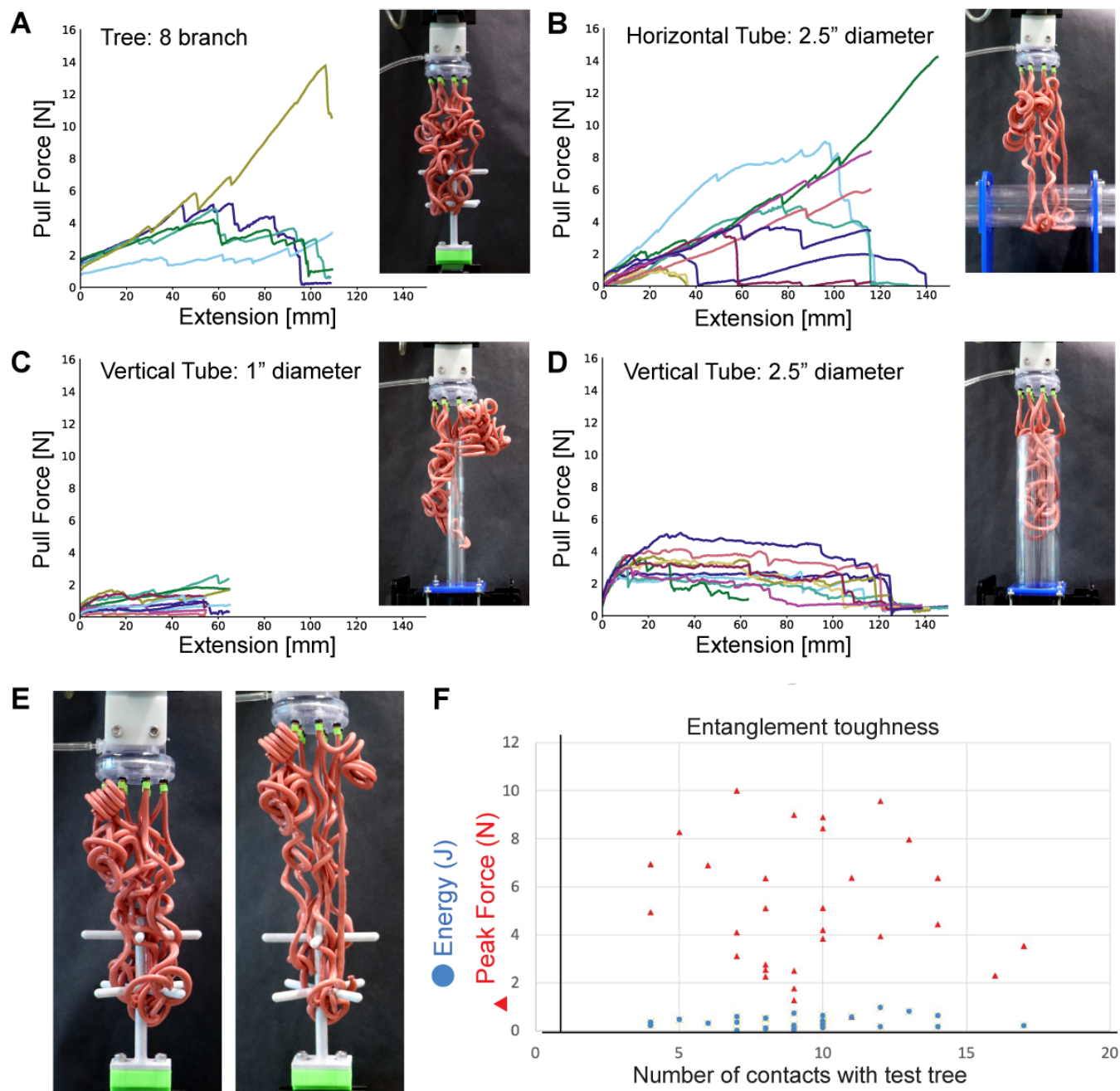


Fig. S4. Grasping force and grasping toughness characterization. Examples of the raw pull force data. The plots show how much force was exerted on an object as it was extracted from a twelve filament entanglement gripper. The corresponding test setup for each plot is shown in the photographs. Objects were rigidly mounted to bottom of test frame and the entanglement gripper was mounted to a load cell on a moving platform above the object. The objects shown are (A) an eight-branch tree, (B) a horizontally oriented 63.5 mm diameter tube, (C) a vertically oriented 25.4 mm diameter tube, and (D) a vertically oriented 63.5 mm diameter tube. (E) Photo of the test tree in the beginning and mid-test of an extraction test. (F) Plot of the entanglement maximum forces and toughness results compared to a manual count of the number of contacts between the filaments and test object.

	Average maximum value [N]	Maximum of maximum values [N]
4 Branch tree	3.92	6.03
8 Branch tree	6.86	16.18
12 Branch tree	9.14	12.66
8 Upward branch tree	2.306	4.68
8 Downward branch tree	5.99	13.42
1"∅ Tube horizontal	6.85	27.64
2.5"∅ Tube horizontal	8.65	34
1"∅ Tube vertical	1.7	5.5
1.5"∅ Tube vertical	6.98	8.64
2.5"∅ Tube vertical	3.77	9.91
Sphere	0.76	2.06

Fig. S5. Maximum values observed in the grasping force tests, including tests shown in Figure S5. The left column contains the average of the maximum values observed for each set of trials and the right column is the maximum value observed over all trials. The trees with branches at 90 degrees to the trunk and the 38.1 mm vertical tube had five trials performed, all other objects had ten trials performed. The upward and downward branch trees are variants of the test tree with the branches angled to 45 deg above and below level. The colors are scaled to the minimum and maximum data values (light green being low and dark green being high values).

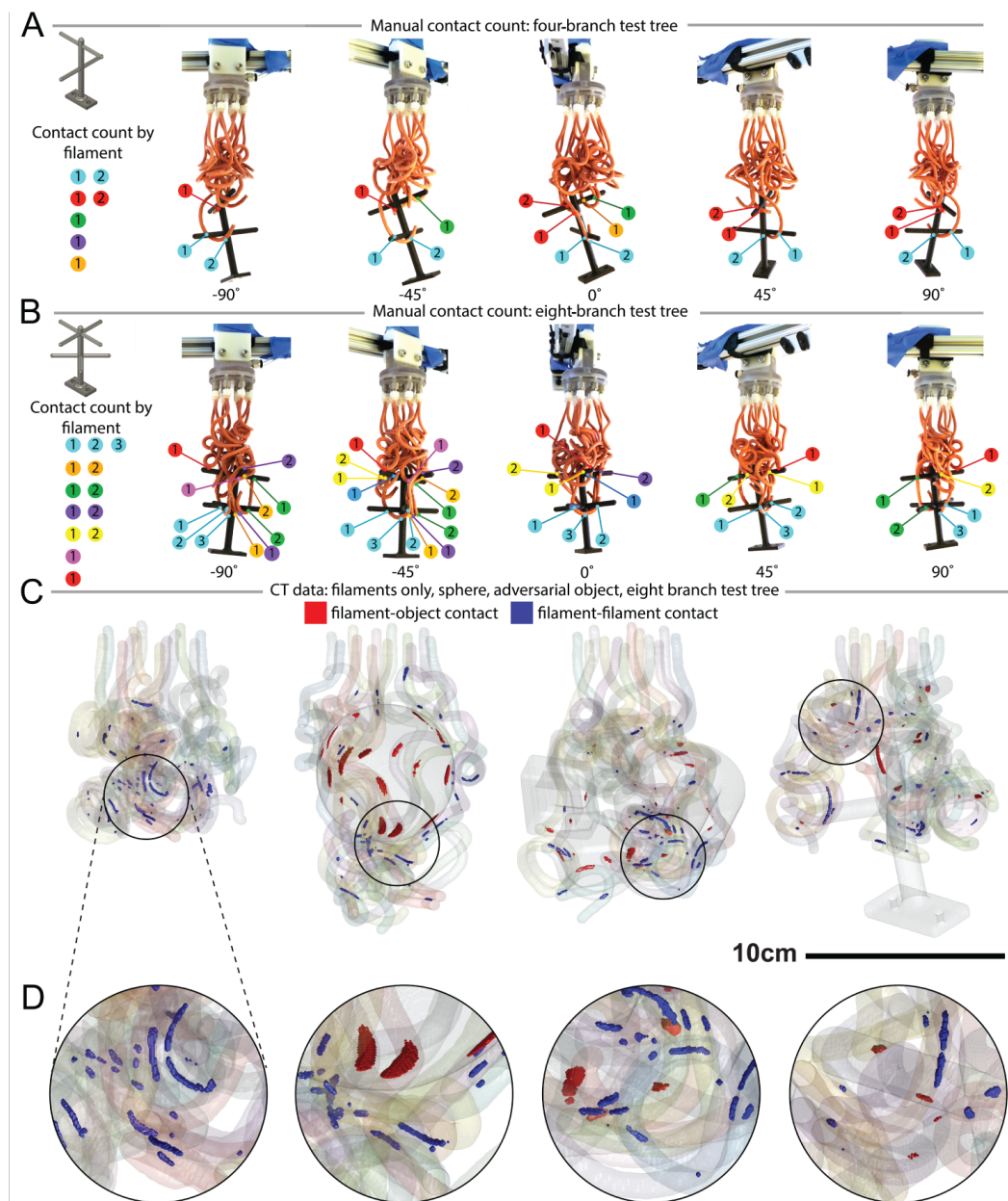


Fig. S6. Spatial distribution of contact points. (A) Manual count of a contact distribution on a four-branch tree. The photographs were taken at five different orientations, each 45 degrees apart. Individual contact points are color coded and grouped by the associated filament. This grasp has seven contact points from five unique filaments of a twelve filament entanglement gripper. (B) Manual count of contact distribution on an eight-branch test tree, which has thirteen contact points from seven unique filaments of a twelve filament entanglement gripper. (C) Contact distribution from micro-CT data with inter-filament contacts indicated in blue and filament-object contacts indicated in red. These are from the same grasp instances shown in Figure 2 of the main text. (D) Zoomed-in contact view of region indicated in C.

Knowing the locations of each contact point, as shown in Figure S6, the contact distribution can be analyzed using a similar approach to that used to calculate the local ACN and spatial density of the filaments. By sweeping a mesoscopic sphere through the space occupied by the gripper, we can count the number of contact points that occur within the sphere. For this work, we continue to use a bounding sphere with a radius of 20mm that is swept through the space of the gripper at an interval of 3.33mm, for all points that intersect the gripper. Given the spacing and radius, there is thus substantial overlap in the bounding volumes represented. The bounding spheres were sampled at 64k grid points (40x40x40) over the full domain of the scan and then spheres that contained no filaments were discarded. The number of sample point represented therefore varies from sample to sample and the histograms of the resulting probability density are normalized such that the area under the curve is 1. The number of grid points for the filaments without an object, for the sphere, for the bar clamp, and for the test tree were 18,735, 14,901, 22,706, and 21,094, respectively.

The probability density for the number of contacts within these bounding spheres is shown in Figure 2F of the main text in parallel with the distribution of local ACN over the same collection of bounding spheres. This plot represents the contacts between filaments in particular to compare the relative entanglement of filaments, but can also include the object-filament

contact points. As mentioned in the main text, we see a correlation between the number of contacts and the measured entanglement. The number of filaments in bounding spheres is also expected to correlate with contacts, so an alternative of this plot is shown in Figure S7, comparing the probability density of filaments for a mesoscopic sphere to the number of contacts. The probability density of contacts is relatively similar between the four different scans presented in Figure 2 of the main text, with slightly more distinction in the probability density of the number of filaments as compared to the ACN. This distinction is attributed to the fact that ACN considers not only how many filaments are nearby, but also the proximity and complexity of their deployed configuration.

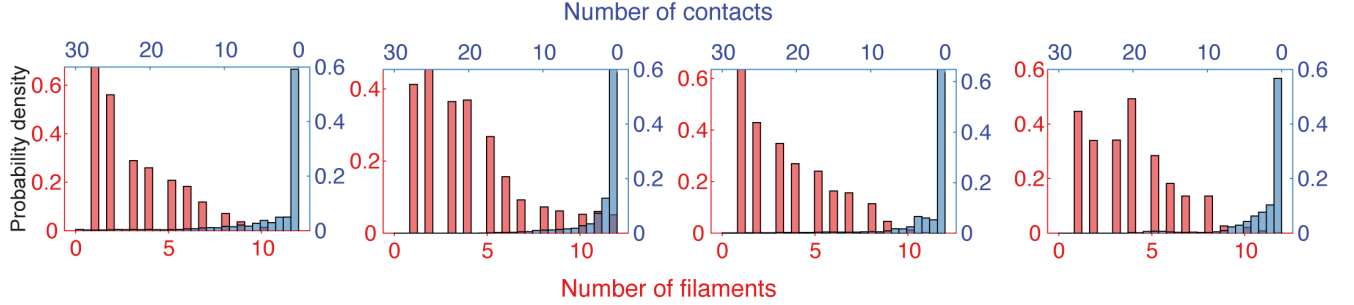


Fig. S7. Probability density of filaments and number of contacts. (A) Similar to Figure 2G in the main text, the blue histogram shows a probability density of the number of contacts within a spherical bounding volume with a 20mm radius. The red histogram shows the probability density for the numbers of filaments contained in the same set of spherical bounding volumes. Each of the four plots corresponds to the example CT scans shown in Figure 2 of the main text, without an object, with a tennis ball, with a bar clamp, and with a test tree.

Adding a spatial element to the analysis of the contact distribution, Figure S8 shows a distribution of the distances between all unique pairs of contact points. The distances are taken between the centroids of the two contact areas. In the presence of an object, the distances tend to increase, which aligns with the intuition that the rigid object introduces a relatively rigid support structure. Normal forces and friction forces at the contact points with the object prevent the filaments from condensing further. With the presence of an object, and in the presence of a more complex object, the upper end of the range of distances between contacts increases. As the contacts are generally spread further, one might expect an increase in stability of a grasp. The spatial distribution of this grasp was measured externally via the micro-CT scan, but one might imagine that proximity sensing within the filaments could also give an internal feedback path to measure grasping stability as well as some degree of object identification.

Looking into the area of contacts, Figure S9 shows the distribution of contact areas as computed by counting the surface voxels of a contact region and multiplying by the area of each voxel. Assuming the object in contact with the filaments is rigid relative to the filaments, the distribution of contact area should correlate to the radius of curvature of the object itself. By adding sensing capability of the filament to detect bulk contact area, this could be used to add information in situ on the curvature and stiffness of an object. It might also be used in conjunction with a tension measurement in the filaments to monitor the effective contact stress on a target object. Overall, we believe further analysis of the array of contacts formed with entangling filaments is a rich area for future exploration, as it pertains to the mechanics of entanglement as well as applications like grasping.

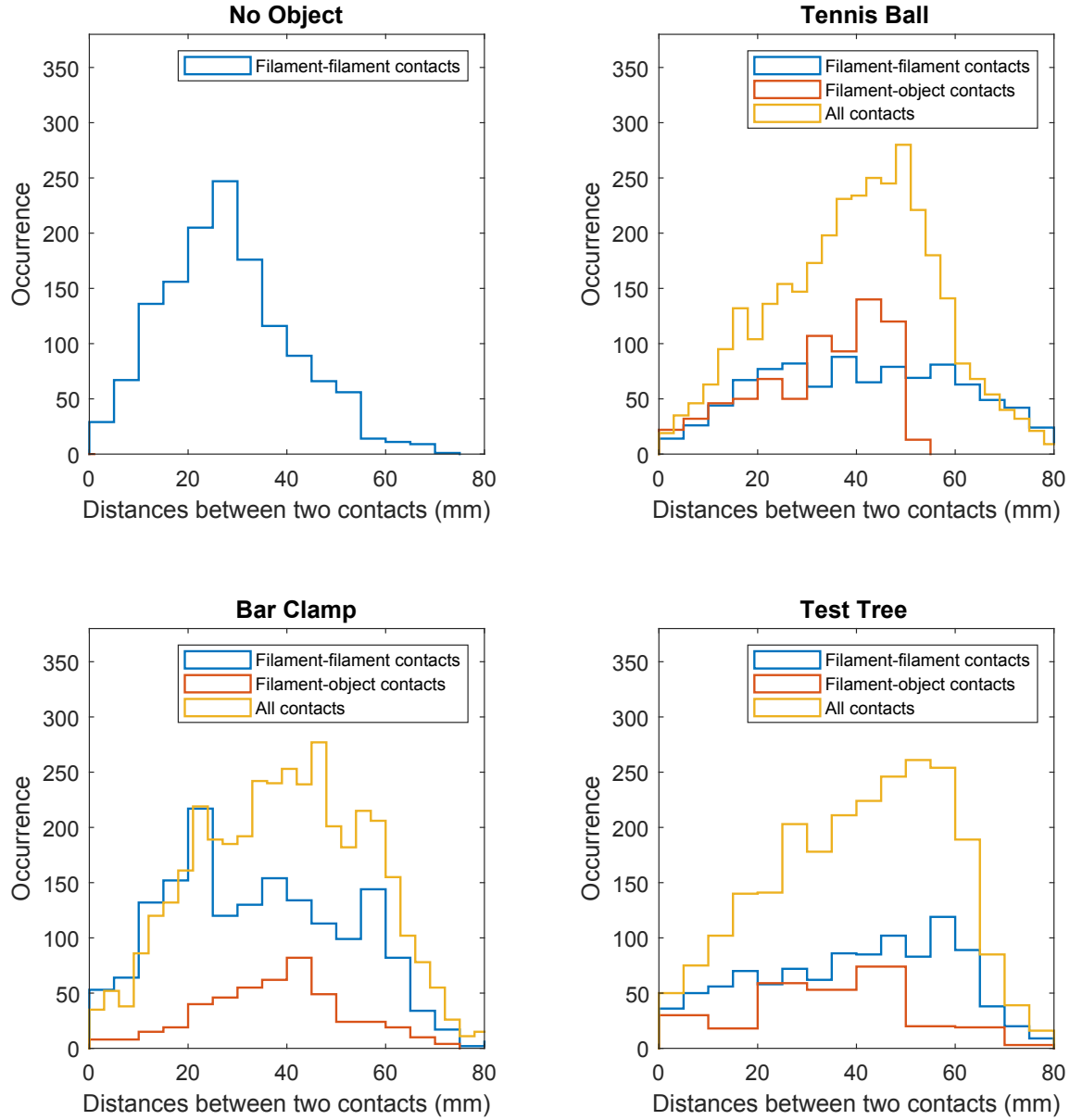


Fig. S8. Statistical analysis of the spatial distribution of contact points. A distribution of the distances between all possible pairs of contact points. Distances are computed between the centroids of contact point detected in the CT scan data. Each of the four plots corresponds to the example CT scans shown in Figure 2 of the main text, without an object, with a tennis ball, with a bar clamp, and with a test tree.

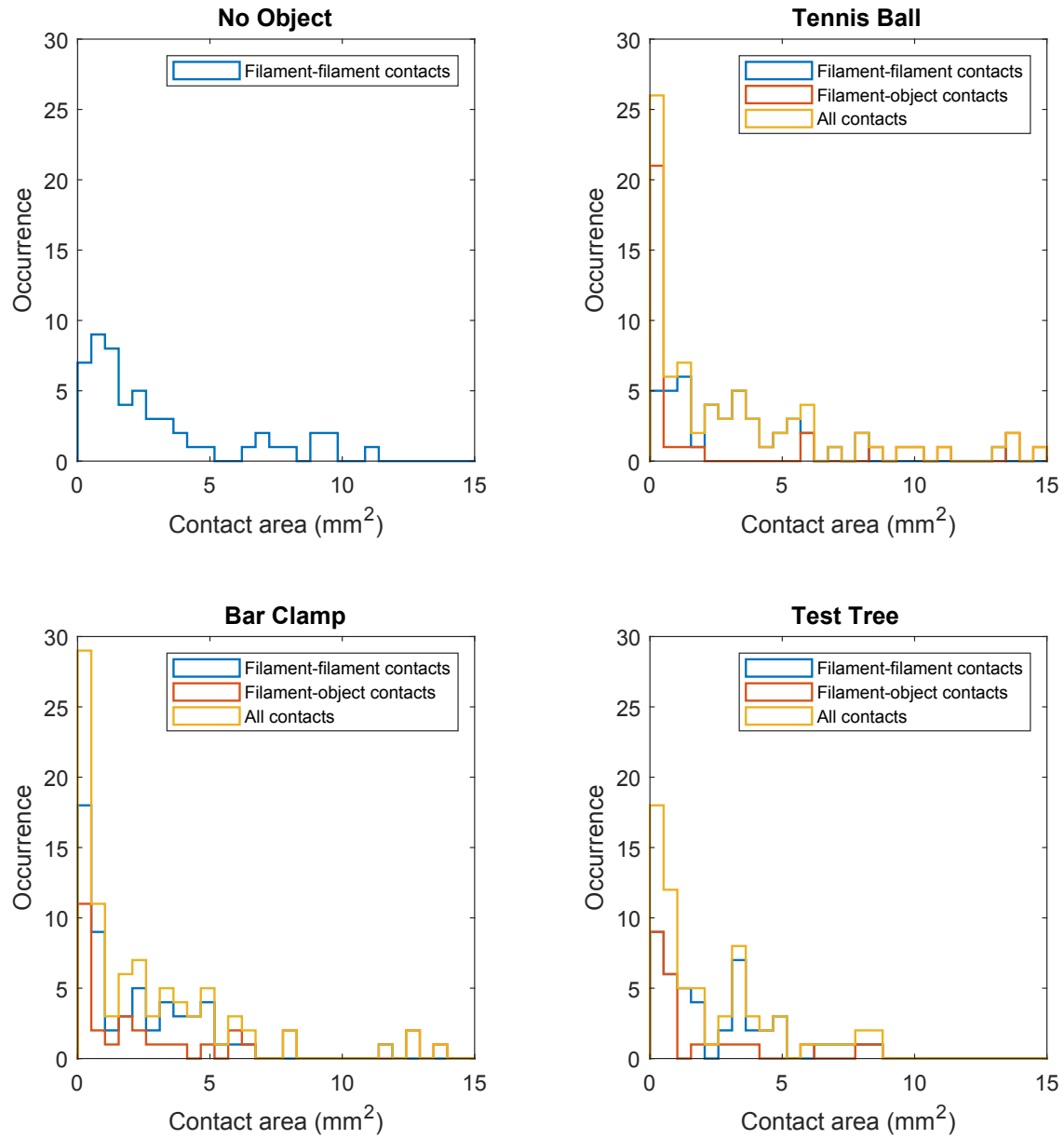


Fig. S9. Statistical analysis of contact area distribution. A distribution of the contact areas achieved, computed via the count of voxels detected in the segmentation of the CT scan data.

Gripper Hardware. The gripper used for all of the physical tests in this work is comprised of twelve silicone filaments attached to a 3D-printed palm, (manifold). The filaments were approximately 260 mm in length and 4.5 mm in diameter prior to actuation. The filaments were mounted to the manifold in one of two ways. First with polypropylene and nylon luer lock plug to barb fittings (McMaster PN51525K141, PN51525K121) on one end and sealed at the other end. The luer lock fittings in the end of the filaments could then be modularly attached to a 3D-printed manifold via nickel coated brass threaded luer lock sockets (McMaster PN51465K161) or 10-32 bolts. The modular Luer lock attachment allowed for modular repairs and convenient replacement of individual filaments in the case of a leak. As a second, alternative means of attachment, 3/32" barb fittings were attached to the manifold and filaments were stretched over and then secured to the barbs with custom FFF (fused filament fabrication) 3D-printed PLA collars. Modular attachment of filaments (via Luer lock connections or the collars) contrast to recent work (8) where the filaments were fabricated as part of an integrated soft structure. The individual ports on the manifold could also be closed with luer lock end plugs (McMaster PN51525K311) for fewer numbers of filaments and easily rearranged for different array formations, although the testing in this study utilized all twelve ports for all of the experiments. The manifold was printed with a transparent resin (Stratysys veroclear OBJ-03271) on a Stratysys Objet30 polyjet 3D printer. Three different mounting attachments were used for (1) mounting to the robot arm for grasp testing, (2) mounting in the materials characterization system (Instron 5544A) the for grip strength tests, and (3) mounting on a ROV for deep-sea tests. For all of the tests, however, the configuration of the ports on the distal portion of the gripper remained the same, and consisted of two concentric circles with evenly spaced ports. The outer circle had diameter 50 mm and contained eight of the twelve ports arranged, while the inner circle had a diameter of 25 mm and contained the remaining four filaments.

Filament Fabrication. The filament actuators in this work were made from silicone rubber, Elastosil m4601 (Wacker Chemie) because of its high elongation to failure (700%), high tearing force, and relatively low cost. The rubber filaments were formed by dip molded silicone onto 305 mm (12 in) long stainless steel pins (McMaster-Carr 88915K11) following the fabrication methods presented by Becker et al.. These methods have been used previously to create actuators up to 1m in length (8). The pins (or rods) were coated with liquid silicone rubber and then fixed at a 10 degree angle from vertical until the rubber is cured to create a thicker coating on one side of the rod. The rods were suspended from above and remained fixed in place between coatings. The filaments used for the tests in this study were formed with four coatings. Once the silicone is cured and the rod is removed, the silicone forms a tube that has a thicker wall on one side where the coating pooled due to gravity. The rubber does not stick to the stainless steel and can be removed without the use of mold release, which is important because mold release could migrate during dipping and would thus create a risk of thin spots and holes in the sidewalls of the actuators. The filaments in this work were formed in batches of 35 because it fit reasonably on the test stand with sufficient spacing to ensure that the curing filaments did not drip on one another, and were not disturbed while coating neighboring filaments. Using this approach, the batch size could easily be scaled up with a larger test stand.

For shorter pins, the full length may be dipped in a cup of rubber and allowed to cure. For long pins, to avoid the need for large dipping vessels and to reduce wasted rubber, a cup with a hole in the bottom was used for the dip coating process. With a hole that is two to three times the diameter of the pin, the rate at which the rubber leaks through the hole is sufficiently low such that it does not drain the cup. By dipping through a cup with a hole in the bottom, we eliminate the need for a tall dipping vessel and reduce wasted rubber. To help with this modified dip coating process for long pins, the pins were suspended from above with enough clearance to freely maneuver the cup below the pins. The cup was held at the top of the pin, filled with uncured rubber, slowly pulled down the length of the pin, and then slid down and off of the lower free end of the pin. The cup could also be filled at the bottom of the pin (or refilled between pins) and pulled up and then down again in the dip coating process, as was done for the batch processing in this work. Pulling the cup down over top-mounted pins, rather than pulling a cup up over bottom-mounted pins, ensures that the rubber is not scraped off of the pin by the edge of the hole in the bottom of the cup; the pin is pulled through the meniscus of the liquid rubber, free from edge effects of the cup.

Various fabrication variables can be altered to tune the functionality of the filament actuators. The angle of pins and number of dip coatings affect the wall thickness and the offset from center of the internal channel of the filaments, which in turn affects the characteristic curvature and operating pressure(8). (A model of the effects of varying the offset of the center channel in a similar structure made with a closed mold form was presented by Gorrisen et al. (9).) The recipe used for the filaments tested in this paper was four dips coatings of the Elastosil rubber, mixed at a 9:1 weight ratio of the two parts, as directed by the product information. The rubber was mixed for two rounds of 30s at 2000 rpm in a planetary centrifugal mixer (Thinky, Laguna Hills, CA, USA), immediately applied to the pins, and then allowed to cure a room temperature before adding another layer. The pins remained fixed at an angle of ten degrees from vertical until fully cured.

Removal of the silicone from the pin was aided by 15-30psi of air pressure applied via a 1/16in hose barb into one side of the silicone. This is most easily done by stretching the tip of the filament off the end of the pin and cutting it off to be able to then insert the barb in the new opening that will be sealed later. It is also possible to slide the barb into the top of the actuator alongside the stainless steel pin. The latter does not create a perfect seal, but supplies enough internal pressure to cause the actuators to expanded and slip off of the pin more easily. This demolding pressure may be modulated depending on the operating pressure of the actuators. Care was taken to apply tension to the actuator during removal from the pin so that, if the barb slipped and the internal pressure dropped, the actuator did not snap back and stretch over the tip of the pin, potentially creating a weak spot or pin hole.

As mentioned above, the filaments can be more easily removed from the pins if the end is also trimmed open and pressurized during the removal process. The open end can then be sealed again using Sil-Poxy (Smooth-On Inc.) or newly mixed Elastosil. For filaments used in the deep-sea field tests, 1/16" diameter, 1/4" long steel pins were inserted into the end before sealing it.

This served the purpose of weighting the ends to make them settle down faster after being moved through the water. The filaments otherwise drift in the water and are harder to direct. The pins also allowed the ends of the filaments to stick to a magnet on the ROV holster to keep them from drifting around until deployment.

After removing the actuators from their forming pins (and sealing one of the two ends if needed), the open end of the filament was fixed onto a plastic 1/16" Luer-lok barb (part listed above) and secured with Sil-Poxy and a wrapping of cotton twine (McMaster-Carr PN1929T12). After all of the Sil-Poxy and rubber is fully set, the Luer-lok fitting could then be attached to the gripper manifold as described above. Alternatively, the filaments in the grasping and toughness tests were stretched over a 1/8" Luer-lok barb and secured in place with 3D-printed collars that slipped over the barb. This allowed for rapid maintenance in the case of a leak. The filaments could be removed from the manifold and replaced in under 10 seconds by manually sliding the collar off, swapping filaments and sliding the collar back on without the need for any tools. The collars were printed on a Flashforge creator pro with an approximate ID of 4.6 mm, OD of 5.2 mm, and length of 5mm. Slight variation on the ID were used for a looser or tighter fit. Examples of the collars can be seen in Figure S4, the bright green fitting at the top of each filament.

Pneumatic Actuation and Control. For repeatable and tuneable actuation of the filaments in the robot arm mounting grasp testing, the input pressure of our filament gripper was controlled by a custom pneumatic pressure control system based on the system used in the studies of Teeple et al. (6) and Abondance et al. (5). The controller enables execution of arbitrary pressure trajectories in real time with an accuracy of 1.4 kPa. The control system used in this work is shown in Figure S10, and only a single actuation channel is used to inflate the gripper. The working control range is between -35 kPa and 350 kPa, and preliminary testing shows this system has a response time of approximately 0.2 s, enabling high-bandwidth operation. Finally, the system utilizes custom ROS drivers allowing high-level coordination between the gripper (pressure controller) and our robot arm.

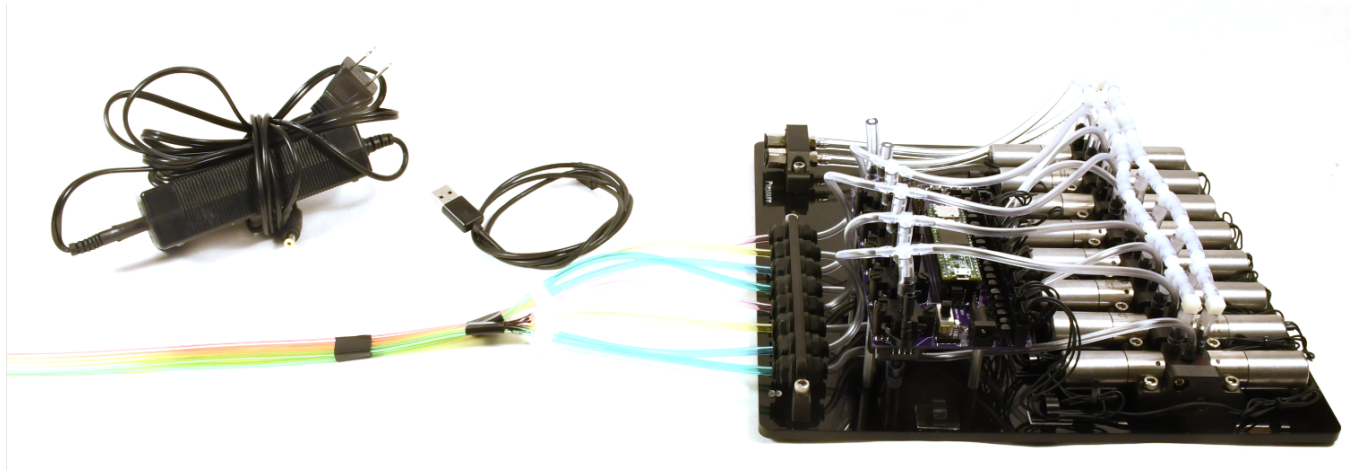


Fig. S10. Control system used in this work is part of an ongoing, open-source project (10). The system can control pneumatic pressure between -35 kPa and 350 kPa with an accuracy of 1.4 kPa and a response time of 0.2 s.

Simulation. We modeled each gripper filament using the Cosserat theory of elastic rods (11, 12), and solved the governing equations using the second order verlet numerical scheme used to model a variety of soft filaments(13). The Cosserat theory allows us to capture the soft nature of the gripper filaments; in particular, it takes into account shear and stretch as well as the more commonly modeled twisting and bending deformation modes. Below, we describe how we applied this simulation scheme to our gripper and eight-branch tree system.

We initialize twelve discretized gripper filaments, suspended vertically with their top ends clamped and all other centerline nodes free. The filaments are subject to gravity and mutual contact forces, including isotropic contact friction. The top ends are arranged in a planar array mimicking experimental setup. Below the plane of the bottom of the hanging gripper filaments, we initialize a branched target structure, mimicking the test tree from the experimental testing. Throughout the simulation, the target is subject to gravity. To keep the target from falling under gravity while the grippers attempt to grasp it, we use two environmental interactions: we simulate an infinite flat plane just below the base of the target's central rod (or "trunk") which interacts with the trunk via a hard contact interaction and contact friction. We also constrain the base of the trunk to remain in a vertical orientation until either (1) the filaments have fully actuated or (2) the base of the trunk is lifted more than $L_t/20$ above the plane, where L_t is the length of the trunk—whichever of those two conditions is met first. Hence, the trunk is kept vertical until the gripper has a chance to grasp the tree, but the tree is not constrained in a way that interferes with grasping.

At the start of a trial, the array of clamped gripper filaments' top ends is lowered until the filaments surround the target. The grippers are actuated by introducing intrinsic curvature everywhere along the length of the filaments at a constant rate, until a prescribed maximum intrinsic curvature is reached. The principal direction of curvature is constant over arclength with

respect to the local filament cross-sectional frames, and is sampled randomly for each filament. The filaments relax elastically to their new state, adapting to their new intrinsic curvature while still being pulled downward by gravity. Note that we do not attempt to model the pressure-curvature relation exhibited by experimental filaments during actuation, but rather simulate actuation by directly prescribing nonzero filament intrinsic curvature.

In particular, the maximum intrinsic curvature varies as a function of arclength, with the maximum curvature value at each node drawn from a Gaussian distribution with mean $\mu_\kappa = 30\pi \frac{1}{m}$ and standard deviation $\sigma_\kappa = \frac{1}{20}\mu_\kappa \frac{1}{m}$. We also introduce a small random twist along the filament, causing small deviations in the principal direction of curvature and introducing a small amount of asymmetry needed for the helical buckling described below. Discretized twist values on each discretization edge are drawn from a Gaussian distribution with mean $0 \frac{1}{m}$ and standard deviation $\pi \frac{1}{m}$. The mean principal direction of curvature (i.e. the direction of curvature with 0 twist insertion) is chosen randomly, as described above. As a result of non-deterministic curvatures, successive simulations with the same system parameters can produce different results. For systems in which the resulting grasp is tenuous, repeated simulations may produce qualitatively, in addition to quantitatively, different results, revealing the precarious nature of the grasp for those system parameters.

As the filaments relax to their new curved state, they initially curl in a nearly planar fashion. As they surpass a critical bending threshold, they buckle under their own weight into helical shapes. Under the correct conditions, filament coiling leads to entanglement between filaments as well as between the filaments and target, leading to a robust grasp, especially for target with complex geometries.

To test grasp success, we lift the gripper upward by displacing the clamped filament ends, keeping the filaments actuated, and observe whether the gripper successfully displaces the target upward and holds it unsupported for a set length of time. We then return the filaments' curvature to zero, releasing the target. Note that if the target and filaments become sufficiently entangled, the target may not fall freely out of the gripper grasp after filament curvature returns to zero.

To simulate branched target structures, we model the trunk and each branch as an elastic filament and fully couple forces and torques at each branch joint. In particular, we initialize the structure's trunk and branches such that, at each joint, the rods being joined at that joint have exactly one node at the joint location. During simulation, the regions of each rod not located at joint locations are simulated as normal elastic rods. To update the positions of rod nodes and edges at joint locations, we first sum the masses, inertia matrices, forces and torques of all nodes and edges at the given joint. Using these summed quantities, we compute an updated position and velocity for the entire joint. We assign this updated joint position and velocity to each node and edge located at that joint. Hence, the nodes from different rods initialized at a given joint location are always updated identically, keeping the joint intact without the use of boundary conditions.

In Tables S1 and S2, we present the simulation parameters used to generate Figure. 3 of the main text and the supplementary video showing example simulations. Note that all parameters were chosen to match experimental measurements. The filaments' cross-section inner radius in the pressurized state is computed to keep the total cross-sectional area constant during actuation, as observed in experiment. Also note that $A_{\text{rest}} = \pi \left(R_{\text{rel}}^o r_{\text{rel}}^o - (r_{\text{rel}}^i)^2 \right)$ denotes cross-sectional area during the relaxed state.

Using the method described in (13) and (14), we use translational and angular linear external damping, and no internal damping. In particular, we apply a linear translational damping force $\mathbf{F}_{\text{damp}} = -(\gamma_t L_f / n_f) \mathbf{v}$, where \mathbf{v} is local filament velocity, L_f is filament length, n_f is filament discretization elements, and γ_t is the translational damping coefficient. Independent of \mathbf{F}_{damp} , we also apply a linear angular damping torque $\mathbf{M}_{\text{damp}} = -(\gamma_a L / n) \boldsymbol{\omega}$, where $\boldsymbol{\omega}$ is the local filament angular velocity and γ_a is the angular damping coefficient. For reference, following the derivation in s(14), we compute characteristic damping scales $\gamma_t^{\text{char}} = r^2 \sqrt{E\pi^3 \lambda / (4L^4)}$ and $\gamma_a^{\text{char}} = L^2 \gamma_t^{\text{char}}$, where λ is mass per unit length and r is radius. For gripper filaments, we use $r = r_{\text{rel}}^o$ and obtain $\gamma_t^{\text{char}} = 1.7 \cdot 10^{-2} \frac{\text{kg}}{\text{m}\cdot\text{s}}$ and $\gamma_a^{\text{char}} = 1.1 \cdot 10^{-3} \frac{\text{kg}\cdot\text{m}}{\text{s}}$. For target trees, we use $L = L_t = 1.2 \cdot 10^{-2} \text{ m}$, $\lambda = \rho_{\text{tree}} \pi \bar{r}_{\text{tree}}^2 = 1.3 \cdot 10^{-1} \text{ kg/m}$, $r = \bar{r}_{\text{tree}}$, where \bar{r}_{tree} is mean tree radius (since tree radius varies over phase space), and ρ_{tree} is tree mass density, to obtain $\gamma_t^{\text{char}} = 9.6 \cdot 10^4 \frac{\text{kg}}{\text{m}\cdot\text{s}}$ and $\gamma_a^{\text{char}} = 13.8 \frac{\text{kg}\cdot\text{m}}{\text{s}}$.

Table S1. Simulation settings for gripper filaments

length L_t	$2.6 \cdot 10^{-1}$ m
inner radius (relaxed) r_{rel}^i	$7.0 \cdot 10^{-4}$ m
outer radius (relaxed, major axis) R_{rel}^o	$2.1 \cdot 10^{-3}$ m
outer radius (relaxed, minor axis) r_{rel}^o	$2.0 \cdot 10^{-3}$ m
inner radius (pressurized) r_{pres}^i	$\sqrt{r_{\text{pres}}^o R_{\text{pres}}^o - (A_{\text{rest}}/\pi)}$
outer radius (pressurized, major axis) R_{pres}^o	$3.1 \cdot 10^{-3}$ m
outer radius (pressurized, minor axis) r_{pres}^o	$2.3 \cdot 10^{-3}$ m
Young's modulus E	$6.2 \cdot 10^5$ Pa
shear modulus G	$E/3$
shear/stretch matrix \mathbf{B}	$\text{diag}(4GA/3, 4GA/3, EA)$ N
bend/twist matrix \mathbf{S}	$\text{diag}(EI_1, EI_2, GI_3)$ Nm ²
discretization elements n_t	130
translational damping γ_t	$2.0 \cdot 10^{-2} \frac{\text{kg}}{\text{m} \cdot \text{s}} = 1.1 \gamma_t^{\text{char}}$
angular damping γ_a	$1.00 \cdot 10^{-2} \frac{\text{kg} \cdot \text{m}}{\text{s}} = 8.6 \gamma_a^{\text{char}}$
mass per unit length λ	$1.6 \cdot 10^{-2}$ kg/m
gravitational strength g	9.8 N/kg
time discretization δt	$\left(0.005 \frac{\text{s}}{\text{m}}\right) L_t/n_t$ seconds

Table S2. Simulation settings for target tree

trunk length L_t	$1.2 \cdot 10^{-1}$ m
mean branch length \bar{L}_b (varies in phase space)	$24\text{em}5 \cdot 10^{-2}$ m
mean trunk radius \bar{r}_{tree}	$5 \cdot 10^{-3}$ m
mean branch radius \bar{r}_{branch}	$3.5 \cdot 10^{-3}$ m
Young's modulus E_{tree}	$3.0 \cdot 10^7$ Pa
shear modulus G	$E/3$
shear/stretch matrix B	$\text{diag}(4GA/3, 4GA/3, EA)$ N
bend/twist matrix S	$\text{diag}(EI_1, EI_2, GI_3)$ Nm ²
trunk discretization elements n_t	15
branch discretization elements n_b	$15L_b/\bar{L}_b$
translational damping γ_t	$2.00 \cdot 10^{-3} \frac{\text{kg}}{\text{m}\cdot\text{s}} = 2.09 \cdot 10^{-8} \gamma_t^{\text{char}}$
angular damping γ_a	$2.00 \cdot 10^{-3} \frac{\text{kg}\cdot\text{m}}{\text{s}} = 1.45 \cdot 10^{-4} \gamma_a^{\text{char}}$
mass density ρ_{tree} (varies in phase space)	$24\text{em}16.67\text{kg/m}^3$
gravitational strength g	9.8 N/kg
time discretization δt	$\left(0.001 \frac{\text{s}}{\text{m}}\right) L_t/n_t$ seconds

Movie S1. The first supplemental movie shows examples of the experimental evaluation of the entanglement grasping strategy, using a UR5 robot arm to pick up various objects while centered as well as with increasing levels of centering offsets.

Movie S2. The second supplemental movie shows the numerical simulations of entanglement grasping strategy with elastic filaments, including a depiction of the parameters that were varied and several examples grasping test simulations.

References

1. B Calli, et al., Benchmarking in manipulation research: Using the yale-cmu-berkeley object and model set. *IEEE Robotics & Autom. Mag.* **22**, 36–52 (2015).
2. DM Aukes, MR Cutkosky, Simulation-based tools for evaluating underactuated hand designs in *2013 IEEE International Conference on Robotics and Automation*. (IEEE), pp. 2067–2073 (2013).
3. NR Sinatra, et al., Ultragentle manipulation of delicate structures using a soft robotic gripper. *Sci. Robotics* **4** (2019).
4. J Mahler, et al., Dex-net 2.0: Deep learning to plan robust grasps with synthetic point clouds and analytic grasp metrics in *Robotics: Science and Systems (RSS)*. (2017).
5. S Abondance, CB Teeple, RJ Wood, A dexterous soft robotic hand for delicate in-hand manipulation. *IEEE Robotics Autom. Lett.* **5**, 5502–5509 (2020).
6. CB Teeple, TN Koutros, MA Graule, RJ Wood, Multi-segment soft robotic fingers enable robust precision grasping. *The Int. J. Robotics Res.* **39**, 1647–1667 (2020).
7. KC Galloway, et al., Soft Robotic Grippers for Biological Sampling on Deep Reefs. *Soft Robotics* **3**, soro.2015.0019 (2016).
8. KP Becker, Y Chen, RJ Wood, Soft actuator arrays: Mechanically programmable dip molding of high aspect ratio soft actuator arrays (adv. funct. mater. 12/2020). *Adv. Funct. Mater.* **30**, 2070075 (2020).
9. B Gorissen, W Vincentie, F Al-Bender, D Reynaerts, M De Volder, Modeling and bonding-free fabrication of flexible fluidic microactuators with a bending motion. *J. Micromechanics Microengineering* **23** (2013).
10. CB Teeple, Ctrl-p: Smooth pressure control for soft robots. *Comput. Softw.* (2020).
11. E Cosserat, F Cosserat, *Théorie des corps déformables*. (A. Hermann et fils,), (1909).
12. OM O'Reilly, *Modeling Nonlinear Problems in the Mechanics of Strings and Rods: The Role of the Balance Laws, Interaction of Mechanics and Mathematics*. (Springer International Publishing, Cham), (2017).
13. M Gazzola, LH Dudte, AG McCormick, L Mahadevan, Forward and inverse problems in the mechanics of soft filaments. *Royal Soc. Open Sci.* **5**, 171628 (2018).
14. N Charles, M Gazzola, L Mahadevan, Topology, geometry, and mechanics of strongly stretched and twisted filaments: Solenoids, plectonemes, and artificial muscle fibers. *Phys. Rev. Lett.* **123**, 208003 (2019).